Available online at www.sciencedirect.com
ScienceDirect
Journal of Computational Physics 221 (2007) 649–665
JOURNAL OF COMPUTATIONAL PHYSICS
www.elsevier.com/locate/jcp

A spectral element least-squares formulation for incompressible Navier–Stokes flows using triangular nodal elements

J.P. Pontaza *

Department of Mechanical Engineering, Texas A&M University, College Station, TX 77843-3123, USA

Received 7 April 2006; received in revised form 12 June 2006; accepted 24 June 2006
Available online 7 September 2006

Abstract

We present a least-squares formulation for the numerical solution of incompressible flows using high-order triangular nodal elements. The Fekete points of the triangle are used as nodes and numerical integration is performed using tensor-product Gauss–Legendre rules in a collapsed coordinate system for the standard triangle. A first-order system least-squares (FOSLS) approach based on velocity, pressure, and vorticity is used to allow the use of practical C^0 element expansions in each triangle. The numerical results demonstrate spectral convergence for smooth solutions, excellent conservation of mass for steady and unsteady problems of the inflow/outflow type, and the flexibility of using triangles to partition domains where the use of quadrangles would be cumbersome or inefficient.

Keywords: Least-squares; Triangles; Incompressible flow; Spectral/*hp* methods

1. Introduction

The numerical solution of the incompressible Navier–Stokes equations using least-squares based finite element models is among the most popular applications of least-squares methods [8]. Least-squares formulations for incompressible flows circumvent the inf–sup condition, thus allowing equal-order interpolation of velocities and pressure, and result (after suitable linearization) in linear algebraic systems with a symmetric positive definite (SPD) coefficient matrix.

Spectral element formulations for incompressible flows using least-squares based models have been presented by Proot and Gerritsma [17], Pontaza and Reddy [14,15], and Heinrichs [6]; where the expected exponential convergence property for smooth solutions has been demonstrated. In addition, good conservation of mass and stability for moderately high Reynolds number unsteady flows has been demonstrated in recent work by Pontaza [16].

* Address: Fluid Flow, Shell Global Solutions (US) Inc., 3333 Hwy. 6 South, Houston, TX 77082, USA. Tel.: +1 281 544 8015.
E-mail address: juan.pontaza@shell.com.

0021-9991/$ - see front matter
doi:10.1016/j.jcp.2006.06.035

Spectral element formulations were originally developed [13] and have been traditionally implemented in a quadrangle (in 2D) or hexahedral (in 3D) based setting, as the multi-dimensional spectral basis is easily constructed by tensor products of the one-dimensional basis. However, in order to handle complex geometries with efficiency the use of triangular elements is preferred.

An efficient approach to construct a C^0 *modal* basis on the triangle by warped tensor products is due to Sherwin and Karniadakis [18], where the quadrangle and its quadrature points are transformed into a triangle by means of a coordinate transformation. Here, we construct a C^0 *nodal* basis using the Fekete points of the triangle [19] as nodes.

The drawback of least-squares formulations is that these have associated with them the requirement of higher regularity of the finite element spaces [15]. The degree of necessary regularity across inter-element boundaries is dictated by the differentiability requirements of the governing equation(s) under consideration and/or the norms used to measure their residuals in the least-squares functional. To reduce the higher regularity requirements and allow the use of practical C^0 element expansions in the least-squares finite element model, the governing equation(s) are first transformed into an equivalent first-order system and the least-squares functional defined by measuring their residuals in terms of L^2 norms only. Transformation of the governing equations to an equivalent first-order system may necessarily imply that additional independent variables need to be introduced, implying an increase in cost. However, the auxiliary variables may be argued to be beneficial as they may represent physically meaningful variables, e.g. vorticity, and will be directly approximated in the model.

Our objective is to demonstrate the use of the triangle based spectral nodal basis in the context of a least-squares formulation for incompressible steady and unsteady flows. We verify the exponential convergence property, test for conservation of mass, and demonstrate the flexibility of using triangular elements in representing geometries where the use of quadrangles would be cumbersome.

An overview of the paper is as follows. In Section 2, we give details on the construction of the triangle based spectral nodal basis. In Section 3, we present the least-squares finite element formulation for the incompressible Navier–Stokes equations. Section 4 is devoted to numerical examples showing: (a) the exponential convergence property of the triangle based nodal spectral basis, (b) good conservation of mass for the least-squares formulation using triangles, and (c) the flexibility of using triangular elements for lid-driven cavity flows in a wedge and flow past two-circular cylinder in a side-by-side arrangement with small surface-to-surface spacing. In Section 5 we present concluding remarks.

2. Nodal expansions in the triangle

To construct a nodal expansion in the triangle we require an optimal set of nodal points and a suitable Lagrange basis through these nodal points. For a quadrangle, these simply result from tensor-products of the one-dimensional Gauss–Lobatto–Legendre (GLL) points and the Lagrange basis going through these optimal points. Here we use a non-tensorial nodal expansion in the triangle.

2.1. Nodal points

A good choice for nodal points in the triangle, are the points that maximize the determinant of the Vandermode matrix, which are known to give a small Lebesgue constant. The Lebesgue constant may be interpreted as a measure of how close the approximation to a function, using the polynomial basis through the chosen nodal points, is to the best approximation in the maximum norm. These points are known as Fekete points; and on the triangle the set consists of $N_t = (p+1)(p+2)/2$ distinct nodal points, where p is the order of the polynomial basis. The Fekete points are independent of the basis used to compute them, as a change in basis simply scales the determinant by a constant.

In the one-dimensional interval $[-1, 1]$, Fekete points are GLL points [1]. Moreover, in the standard square and cube the Fekete points are the tensor-product of the GLL points [1]; and on the sides of the standard triangle, the Fekete points are GLL points [19]. This nice property allows for conforming meshes of triangles and quadrangles. The Fekete points have been accurately computed for the triangle, up to $p = 19$, by Taylor et al. [19]. They observed that the Lebesgue constant using the Fekete points behaved as $\sqrt{N_t}$, while for equispaced points the Lebesgue constant is known to increase exponentially. Hence, the optimality of the Fekete points.

2.2. Lagrange basis

There is no closed-form expression for the Lagrange basis through sets of points in the triangle, so we express the basis in terms of another basis which has a closed-form definition. This is possible, as long as both basis span the same polynomial space. Ultimately, to obtain the Lagrange basis, a matrix inversion of the Vandermode matrix associated with the closed-form basis is needed; thus the choice of the basis is important as it will dictate the conditioning of the Vandermode matrix.

In the standard triangle,

$$T = \{(\xi,\eta)| -1 \leqslant \xi,\eta \leqslant 1;\ \xi+\eta \leqslant 0\}$$

we use the following orthogonal polynomial [3],

$$\phi_{mn}(\xi,\eta) = P_m^{0,0}(\hat{\xi})\left(\frac{1-\hat{\eta}}{2}\right)^m P_n^{2m+1,0}(\hat{\eta}) \tag{1}$$

with $\hat{\xi} = 2(1+\xi)/(1-\eta) - 1$, $\hat{\eta} = \eta$, and $\{(m,n)|m,n \geqslant 0;\ m+n \leqslant p\}$ for a total of $1,2,3,\ldots,N_t = (p+1)(p+2)/2$ modes in the basis, where p is the order of the polynomial basis. In (1), $P_k^{\alpha,\beta}$ are Jacobi polynomials of order k.

For a unique bijection $j = j(m,n)$, we define the (generalized) Vandermode matrix as $V_{ij} = \phi_j(\boldsymbol{\xi}_i)$, where $\boldsymbol{\xi}_i = (\xi_i,\eta_i)$ are chosen nodal points in the triangle (in our case, the Fekete points) and $\dim(V_{ij}) = N_t \times N_t$. The Lagrange basis $\{L_j\}_{j=1}^{N_t}$ at any point $\boldsymbol{\xi} \in T$ is obtained by performing a collocation projection:

$$\phi_i(\boldsymbol{\xi}) = \sum_{j=1}^{N_t} \phi_j(\boldsymbol{\xi}_i)L_j(\boldsymbol{\xi}) = \sum_{j=1}^{N_t} V_{ij}L_j(\boldsymbol{\xi})$$

or in matrix notation

$$\{\phi(\boldsymbol{\xi})\} = [V]\{L(\boldsymbol{\xi})\}$$

and consequently

$$\{L(\boldsymbol{\xi})\} = [V]^{-1}\{\phi(\boldsymbol{\xi})\}$$

where $[V]^{-1}$ denotes the inverse of the Vandermode matrix $[V]$ with entries V_{ij} defined earlier. Fig. 1 shows selected vertex, edge, and interior members of the $p = 9$ Lagrange basis. The Kronecker-delta property of the Lagrange basis is evident from the plots.

The derivatives of the Lagrange basis are computed in a similar fashion, as follows:

$$\left\{\frac{\partial L}{\partial \xi}(\boldsymbol{\xi})\right\} = [V]^{-1}\left\{\frac{\partial \phi}{\partial \xi}(\boldsymbol{\xi})\right\}, \quad \left\{\frac{\partial L}{\partial \eta}(\boldsymbol{\xi})\right\} = [V]^{-1}\left\{\frac{\partial \phi}{\partial \eta}(\boldsymbol{\xi})\right\}$$

In practice, these operations are performed only once in a pre-processing stage for the master element.

2.3. Numerical integration

In the resulting least-squares formulation, among other types of inner products, it will be necessary to evaluate inner products of the form

$$(L_i, L_j) = \int_T L_i(\xi,\eta)L_j(\xi,\eta)J(\xi,\eta)\,\mathrm{d}\xi\,\mathrm{d}\eta$$

where $L_i, L_j \in \mathbb{P}^p$ and $J(\xi,\eta)$ is the Jacobian of the transformation $\Omega^e \in (x,y) \rightleftarrows T \in (\xi,\eta)$. For the general case of curved elements, the Jacobian will not be constant over the triangle.

For quadrangles, integrals are efficiently computed using the tensor-product of the Gauss–Legendre quadrature points and weights. Using a pth order Gauss–Legendre quadrature rule over the quadrangle, exactly integrates the product $L_iL_j \in \mathbb{P}^{2p+1}$. Unfortunately, there is no obvious analogue set of weights for the Fekete points that will achieve the same level of accuracy.

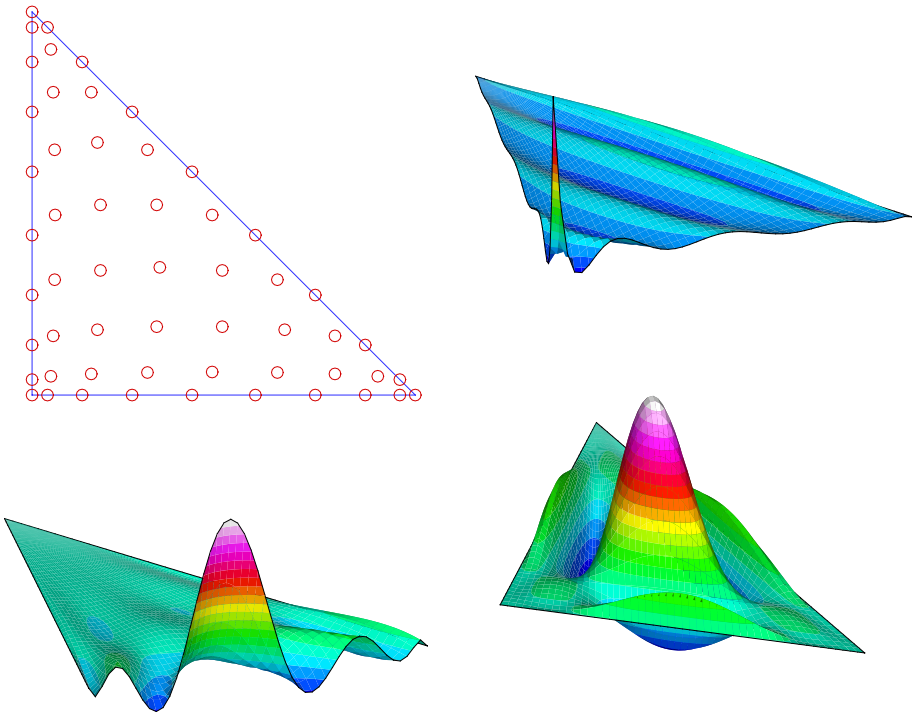

Fig. 1. The standard triangle and its Fekete points for $p = 9$. Selected vertex, edge, and interior shape functions of the Lagrange basis.

The quadrature weights proposed by Taylor et al. [19] for use with the Fekete points are exact for $L_i L_j \in \mathbb{P}^p$, which is not sufficient. The set of weights used by Warburton et al. [20] and Pasquetti and Rapetti [12] are exact for $L_i L_j \in \mathbb{P}^{2p}$, but valid only for a constant Jacobian, i.e. straight sided elements.

Here we use a tensor-product of the Gauss–Legendre quadrature points and weights in the collapsed coordinate system

$$\widehat{T} = \{(\hat{\xi}, \hat{\eta}) | -1 \leqslant \hat{\xi}, \hat{\eta} \leqslant 1\}$$

with $\hat{\xi} = 2(1+\xi)/(1-\eta) - 1$, $\hat{\eta} = \eta$. Unlike the standard triangular region T, the bounds on the region $\widehat{T}$ are no longer dependent on each other.

In the collapsed coordinate system the inner product is written as

$$(L_i, L_j) = \int_{-1}^{+1} \int_{-1}^{+1} L_i(\hat{\xi}, \hat{\eta}) L_j(\hat{\xi}, \hat{\eta}) J(\hat{\xi}, \hat{\eta}) \frac{1-\hat{\eta}}{2} \, \mathrm{d}\hat{\xi} \, \mathrm{d}\hat{\eta}$$

and can be easily evaluated using the tensor-product of the Gauss–Legendre quadrature points and weights. Here we use $p+1$ Gauss–Legendre quadrature points in each collapsed coordinate direction. As an added bonus, since the Gauss–Legendre quadrature points do not include the end points of the interval $[-1,+1]$, no special attention is needed in evaluating derivatives of ϕ_{mn} at the end point $\eta = +1$ of the standard triangle.

This approach is the one developed by Sherwin and Karniadakis [18] for use with modal expansions in the triangle, albeit they use a Gauss–Lobatto–Legendre quadrature in the $\hat{\xi}$ direction and a Gauss–Radau–Jacobi quadrature in the $\hat{\eta}$ direction, which absorbs the Jacobian term $(1-\hat{\eta})/2$ and also avoids the point $\eta = +1$ of the standard triangle.

3. Least-squares formulation for the incompressible Navier–Stokes equations

Let $\bar{\Omega}$ be the closure of an open bounded region Ω in $\mathbb{R}^d$, where $d = 2$ or 3 represents the number of space dimensions, and $\mathbf{x} = (x_1, \ldots, x_d) = (x, y, z)$ be a point in $\bar{\Omega} = \Omega \cup \partial\Omega$, where $\partial\Omega = \Gamma$ is the boundary of Ω. We consider the solution of the Navier–Stokes equations, which in dimensionless form can be stated as follows.

Find the velocity $\mathbf{u}(\mathbf{x},t)$ and pressure $p(\mathbf{x},t)$ such that

$$\frac{\partial \mathbf{u}}{\partial t} + (\mathbf{u}\cdot\nabla)\mathbf{u} + \nabla p - \frac{1}{Re}\Delta\mathbf{u} = \mathbf{0} \quad \text{in } \Omega\times(0,\tau] \tag{2}$$

$$\nabla\cdot\mathbf{u} = 0 \quad \text{in } \bar{\Omega}\times(0,\tau] \tag{3}$$

$$\mathbf{u}(\mathbf{x},0) = {}^0\mathbf{u}(\mathbf{x}) \quad \text{in } \Omega \tag{4}$$

$$\mathbf{u} = \mathbf{u}^s(\mathbf{x},t) \quad \text{on } \Gamma_u\times(0,\tau] \tag{5}$$

where $\Delta = \nabla^2$, Re is the Reynolds number, and in Eq. (4) the initial conditions are given. A well posed problem requires $\nabla\cdot{}^0\mathbf{u} = 0$ in $\bar{\Omega}$. If $\Gamma = \Gamma_u$, the pressure may only be determined up to a constant in which case the average pressure is set to zero.

For ease of exposition, we consider the stationary Stokes problem with homogeneous boundary conditions. In other words, we drop the nonlinearity and the transient term momentarily to present the least-squares formulation. The resulting Stokes problem (with $Re = 1$) is given by:

$$-\Delta\mathbf{u} + \nabla p = \mathbf{0} \quad \text{in } \Omega \tag{6}$$

$$\nabla\cdot\mathbf{u} = 0 \quad \text{in } \bar{\Omega} \tag{7}$$

$$\mathbf{u} = \mathbf{0} \quad \text{on } \Gamma \tag{8}$$

To define the variational problem, we will make use of the following spaces:

$$H_0^s(\Omega) = \{v\in H^s(\Omega) | v = 0 \quad \text{on } \Gamma\}$$

$$\bar{H}^s(\Omega) = \{q\in H^s(\Omega) | \int_\Omega q\,\mathrm{d}\Omega = 0\}$$

for $s \geqslant 0$, with $H^0(\Omega) = L^2(\Omega)$.

3.1. Weak form Galerkin formulations

Before presenting the least-squares formulation, we briefly review formulations using the traditional weak form Galerkin approach. This will allow us to draw some comparisons between the formulations.

In the weak form Galerkin approach, the variational from of the Stokes problem is written as

$$(\nabla\mathbf{u},\nabla\mathbf{v}) - (p,\nabla\cdot\mathbf{v}) = 0 \quad \forall\mathbf{v}\in[H_0^1(\Omega)]^d \tag{9}$$

$$-(\nabla\cdot\mathbf{u},q) = 0 \quad \forall q\in\overline{L}^2(\Omega) \tag{10}$$

where $(\cdot,\cdot)$ are suitable L^2 inner products, and we have arranged the inner products such that the resulting matrix blocks associated with the velocity and pressure are readily identified. We note that the resulting linear algebraic system generated by the forms will have a diagonal zero block; making the global matrix symmetric and indefinite.

The variational problem is a saddle-point problem, where the field p (the pressure) acts as a Lagrange multiplier enforcing the incompressibility condition. Choosing appropriate finite element spaces of the function spaces for the saddle-point problem is not trivial, as these must satisfy the well-known inf–sup, or Ladyzhenskaya–Babuska–Brezzi (LBB), condition [4].

The projection associated with the saddle-point problem may be improved by changing the previously zero diagonal block to a positive definite block; by making use of the regularized divergence-free constraint $\nabla\cdot\mathbf{u} = -\varepsilon p$, with $0<\varepsilon<1$. This leads to the following variational form of the (now regularized) Stokes problem:

$$(\nabla\mathbf{u},\nabla\mathbf{v}) - (p,\nabla\cdot\mathbf{v}) = 0 \quad \forall\mathbf{v}\in[H_0^1(\Omega)]^d \tag{11}$$

$$(\nabla\cdot\mathbf{u},q) + (\varepsilon p,q) = 0 \quad \forall q\in\overline{L}^2(\Omega) \tag{12}$$

In this approach, the parameter ε must be chosen sufficiently small to adequately enforce the incompressibility condition. Moreover, the finite element spaces for the velocity and pressure must still satisfy the inf–sup (LBB)

condition. Solutions of the above regularized problem approach solutions of the (true) Stokes problem at a rate $\mathcal{O}(\varepsilon)$ [5]. In the limit $\varepsilon \to 0$ one simply recovers the exact divergence-free constraint.

The rate at which solutions of the regularized problem approach solutions of the (true) Stokes problems may be improved dramatically to $\mathcal{O}(\varepsilon^k)$, by using the following form [5]:

$$(\nabla \cdot \mathbf{u}, q) + (\varepsilon p^{(k)}, q) = (\varepsilon p^{(k-1)}, q) \quad \forall q \in \overline{L}^2(\Omega) \tag{13}$$

The linear problem, now becomes a quasi-nonlinear problem due to the iterative nature of the regularization. The additional cost incurred becomes negligible when dealing with the Navier–Stokes equations, where the convective terms must be linearized as well.

In practice, the above regularized (weak form Galerkin) formulations are rarely used as they do not offer significant improvement over the non-regularized variational problem. However, as we discuss in the following, regularized formulations offer significant advantages in the least-squares setting.

3.2. Least-squares formulation

In the least-squares approach, the variational problem is such that the velocity field and pressure field minimize the sum of the squares of the residuals of the governing equations measured in the L^2 norm. The associated functional is given by

$$\mathscr{J}(\mathbf{u}, p) = \frac{1}{2}\|-\Delta\mathbf{u} + \nabla p\|^2_{L^2(\Omega)} + \frac{1}{2}\|\nabla \cdot \mathbf{u}\|^2_{L^2(\Omega)} \tag{14}$$

Taking the first variation of the above functional with respect to $\mathbf{u}$ and p and setting it to zero, yields the following variational form of the Stokes problem:

$$(\Delta\mathbf{u}, \Delta\mathbf{v}) + (\nabla \cdot \mathbf{u}, \nabla \cdot \mathbf{v}) - (\nabla p, \Delta\mathbf{v}) = 0 \quad \forall \mathbf{v} \in [H^2_0(\Omega)]^d \tag{15}$$

$$-(\Delta\mathbf{u}, \nabla q) + (\nabla p, \nabla q) = 0 \quad \forall q \in \bar{H}^1(\Omega) \tag{16}$$

A notable property of the resulting global coefficient matrix is that it is symmetric and positive definite (SPD). In addition, the finite element spaces for velocity and pressure are not subject to the inf–sup (LBB) condition [8].

If we compare the least-squares variational problem with that from the weak form Galerkin approach, we see that in the least-squares variational problem there is an inherent lack of velocity–pressure coupling, as the pressure does not appear in any of forms acting as a Lagrange multiplier enforcing the divergence free-constraint.

In [16], Pontaza demonstrated improved velocity–pressure coupling (and improved conservation of mass) for least-squares formulations of incompressible flows by using the regularized form of the incompressibility condition. Such an approach leads to the following variational problem:

$$(\Delta\mathbf{u}, \Delta\mathbf{v}) + (\nabla \cdot \mathbf{u}, \nabla \cdot \mathbf{v}) - (\nabla p, \Delta\mathbf{v}) + \underline{(\varepsilon p, \nabla \cdot \mathbf{v})} = 0 \quad \forall \mathbf{v} \in [H^2_0(\Omega)]^d \tag{17}$$

$$-(\Delta\mathbf{u}, \nabla q) + \underline{(\nabla \cdot \mathbf{u}, \varepsilon q)} + (\nabla p, \nabla q) + \underline{(\varepsilon p, \varepsilon q)} = 0 \quad \forall q \in \bar{H}^1(\Omega) \tag{18}$$

The underlined terms are the additional terms due to the use of the regularized divergence-free constraint and are responsible for the improved velocity–pressure coupling. The terms closely resemble those found in the weak form Galerkin approach, where pressure acts as a Lagrange multiplier enforcing the incompressibility constraint. Specifically we see that the off-diagonal blocks are augmented with forms enhancing the velocity–pressure coupling, where the pressure is acting as a Lagrange multiplier enforcing the incompressibility condition, and the diagonal pressure block is augmented with a scaled mass matrix. Like before, the resulting global coefficient matrix is SPD and the finite element spaces for velocity and pressure are not subject to the inf–sup condition.

As in the Galerkin approach, it is to be noted that solutions of the regularized problem approach solutions of the (true) Stokes problem at a rate $\mathcal{O}(\varepsilon)$. Pontaza [16] used the iterative regularization approach, which improves the rate to $\mathcal{O}(\varepsilon^k)$. In other words, the formulation is consistent up to $\mathcal{O}(\varepsilon^k)$, which can be made arbitrarily small.

Pontaza [16] made use of $\varepsilon = 0.01$, with up to $k = 1, 2, \ldots, 5$ regularization steps. As alluded to earlier, the additional cost incurred due to the iterative regularization becomes negligible when dealing with the Navier–Stokes equations, as the iterative regularization is embedded and made one with the iterative linearization of the convective terms.

An important and attractive property of this formulation is that, for unsteady problems, the dependence of the condition number on the time step size is largely suppressed [16]. This is beneficial, as the solvers of choice are conjugate gradient algorithms, whose rate of convergence strongly depend on the conditioning of the global coefficient matrix. We adopt this formulation in the work herein. Additional details of the formulation may be found in [16].

3.3. First-order system least-squares

The drawback of least-squares formulations is that these have associated with them the requirement of higher regularity of the finite element spaces. The degree of necessary smoothness is dictated by the differentiability requirements of the governing equation(s) under consideration. For the Stokes problem at hand $\mathbf{u} \in [H_0^2(\Omega)]^d$ and $p \in \bar{H}^1(\Omega)$. The higher regularity requirements stem from the fact that the integration by parts step in weak form Galerkin formulations, is absent in least-squares formulations.

To reduce the higher regularity requirements, the governing equation(s) are first transformed into an equivalent first-order system. Transformation of the governing equations to an equivalent first-order system necessarily implies that additional independent variables need be introduced, implying an increase in cost. However, the auxiliary variables may be argued to be beneficial as they may represent physically meaningful variables, e.g. vorticity or stresses, and will be directly approximated in the model.

The first-order system least-squares (FOSLS) approach renders the formulation *practical*, in the sense that existing computational frameworks based on C^0 expansions are easily adapted to the least-squares formulations. In addition, the conditioning of the coefficient matrices is lowered as only first-order operators are involved. Here we use a first-order system based on velocity, pressure, and vorticity.

In view of the identity $\Delta\mathbf{u} = -\nabla\times(\nabla\times\mathbf{u}) + \nabla(\nabla\cdot\mathbf{u})$ and the incompressibility condition, the FOSLS functional for the (non-regularized, i.e. true) Stokes problem is

$$\mathscr{J}(\mathbf{u}, p, \boldsymbol{\omega}) = \frac{1}{2}\|\nabla\times\boldsymbol{\omega} + \nabla p\|^2_{L^2(\Omega)} + \frac{1}{2}\|\nabla\cdot\mathbf{u}\|^2_{L^2(\Omega)} + \frac{1}{2}\|\boldsymbol{\omega} - \nabla\times\mathbf{u}\|^2_{L^2(\Omega)} \tag{19}$$

for $\mathbf{u} \in [H_0^1(\Omega)]^d$, $p \in \bar{H}^1(\Omega)$, and $\boldsymbol{\omega} \in [H^1(\Omega)]^{2d-3}$. We note that no additional or fictitious boundary conditions for the auxiliary variables are needed, as these variables are simply used to reduce differentiability requirements and not used to replace the primitive variables (velocity and pressure).

3.4. Time stepping and nonlinearities

When using the non-stationary (unsteady) form of the equations, the transient terms are represented by a stiffly-stable second-order scheme (a BDF2 scheme):

$$\frac{\partial\mathbf{u}}{\partial t} \approx \frac{1}{\Delta t}\left(\frac{3}{2}\mathbf{u}^{s+1} - 2\mathbf{u}^{s} + \frac{1}{2}\mathbf{u}^{s-1}\right)$$

where $\Delta t = t_{s+1} - t_s$ is the time increment, and it is implied that the problem will march in time. Once the temporal approximation has been introduced the momentum equations are written as $\mathbf{u}^{s+1} - \Delta t\mathbf{L} = \mathbf{0}$, for the time stepping. The BDF2 time stepping scheme is non-self starting, so the first time step is taken using a BDF1 scheme (which is the backward Euler scheme).

In the Navier–Stokes equations, the nonlinear convective terms are linearized around $\mathbf{u}_0$ using Newton's method

$$(\mathbf{u}\cdot\nabla)\mathbf{u} \approx (\mathbf{u}_0\cdot\nabla)\mathbf{u} + (\mathbf{u}\cdot\nabla)\mathbf{u}_0 - (\mathbf{u}_0\cdot\nabla)\mathbf{u}_0$$

At each time step, we iteratively solve a linearized system of algebraic equations with respect to the Newton linearization. In turn, at each nonlinear iteration, the system of linear algebraic equations may be solved using

a direct method (e.g. Cholesky factorization) or an iterative method (e.g. preconditioned conjugate gradient). Here, we use a matrix-free conjugate gradient algorithm with a Jacobi preconditioner. Convergence of the PCG iterative algorithm is declared when the discrete L^2 norm associated with the residual vector of the linear algebraic equations is less than 10^{-6}.

On a given time step, nonlinear convergence in velocities is declared when the criterion

$$\frac{\|\delta \mathbf{u}\|}{\|\mathbf{u}\|} = \frac{\|\mathbf{u}^{(k)} - \mathbf{u}^{(k-1)}\|}{\|\mathbf{u}^{(k)}\|} < 10^{-4}$$

is satisfied; where $\|\mathbf{u}^{(k)}\|$ denotes the discrete L^2 norm of the velocity vector at the kth nonlinear iteration on a given time step. When using the regularized form of the divergence-free constraint, convergence of the pressure field is also monitored due to the iterative regularization, and is declared when $\|\delta p\|/\|p\| < 10^{-3}$. Since the regularization/linearization steps are embedded in each other, both criteria need to be satisfied to declare nonlinear convergence. When using a small time step size, the criteria is satisfied in at most two or three linearization steps. However, the number of steps till convergence is also largely dependent on the flow field and Reynolds number.

4. Numerical examples

4.1. Verification: Kovasznay flow

The benchmark problem to be used for the purposes of verification is an analytic solution to the two-dimensional, stationary incompressible Navier–Stokes due to Kovasznay [11]. The spatial domain in which Kovasznay's solution is defined is taken here as the bi-unit square $\bar{\Omega} = [-0.5, 1.5] \times [-0.5, 1.5]$. The solution is given by

$$\begin{aligned} u(x,y) &= 1 - \mathrm{e}^{\lambda x}\cos(2\pi y) \\ v(x,y) &= \frac{\lambda}{2\pi}\mathrm{e}^{\lambda x}\sin(2\pi y) \\ p(x,y) &= p_0 - \frac{1}{2}\mathrm{e}^{2\lambda x} \end{aligned} \tag{20}$$

where $\lambda = Re/2 - (Re^2/4 + 4\pi^2)^{1/2}$, p_0 is a reference pressure (an arbitrary constant), and we choose $Re = 40$.

We perform a p-refinement study, where we choose and fix a spatial discretization $\bar{\Omega}^h$, and systematically increase the p-level of the element basis. Fig. 2 shows the discretization of the domain, consisting of 16 triangles. Having chosen appropriate error measures, these measures should decay exponentially fast as the p-level is increased. In a logarithmic-linear scale the expected rate of convergence would appear as a straight line.

By 'appropriate error measures', we mean the L^2 and H^1 norms of the difference between the numerical solution and the exact solution given by Eq. (20); in addition to the value of the L^2 least-squares functional. These are appropriate error measures to convincingly show that the least-squares formulation delivers solutions to the incompressible Navier–Stokes equations, i.e. verification.

The exact solution, given by Eq. (20), is used to prescribe Dirichlet velocity boundary conditions on Γ and pressure is specified at a point. No boundary conditions for the vorticity are necessary. In Fig. 2 we plot the value of the L^2 least-squares functional and L^2 error of the velocity, pressure, and vorticity fields as a function of the expansion order in a logarithmic-linear scale. Exponentially fast decay (spectral convergence) of the L^2 least-squares functional and L^2 error is observed.

To make a direct comparison of the behavior of the error measures using quadrangles and triangles, we note that the error measures in Fig. 2 for even p-levels correspond to those obtained using the mesh of triangles and those for odd p-levels to a mesh of eight quadrangles; obtained by joining pairs of triangular elements along the edge opposite the right angle. The numerical results using quadrangles are directly taken from our previous work [14]. We see that both approaches give the desired spectral convergence and a similar rate of decay of error values.

Note that the spectral convergence of the least-squares functional automatically implies exponentially fast decay of the divergence of the velocity field. In addition we note that the least-squares functional gives an

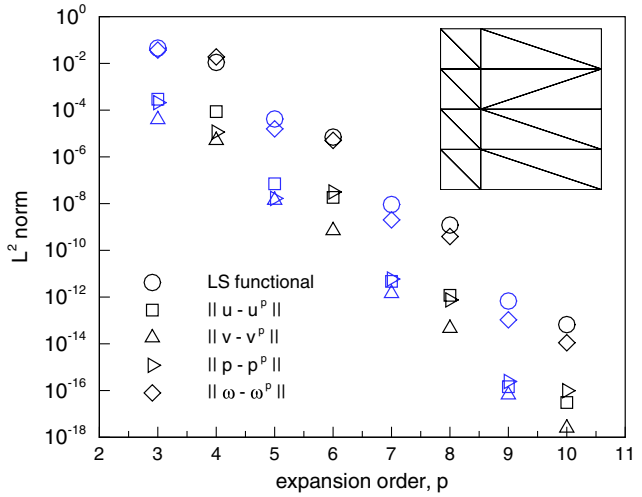

Fig. 2. Decay of the least-squares functional and convergence of the velocity, pressure, and vorticity fields to the Kovasznay solution in the L^2 norm. Even p-level error measures are for the mesh of triangles and odd p-level error measures are for a mesh of quadrangles.

upper-bound for the L^2 error of the velocity and pressure. In the absence of an exact solution (which is always the case for problems of interest) the value of the least-squares functional provides a valuable sharp estimate of the error.

Fig. 3 shows the error of the velocity and pressure fields measured in H^1. This error measure is more stringent than that measured in L^2. Exponentially fast decay (spectral convergence) of the H^1 error is observed.

4.2. Lid-driven flow in a wedge

We consider the lid-driven incompressible flow inside a wedge of aspect ratio $2\sqrt{3}:3$ (a $2\sqrt{3}$ equilateral triangle). In this geometry the use of quadrangles is problematic, whereas the use of triangles is quite natural. Our aim in presenting numerical results for this problem is to demonstrate the flexibility and ease of using triangles to partition such a geometry.

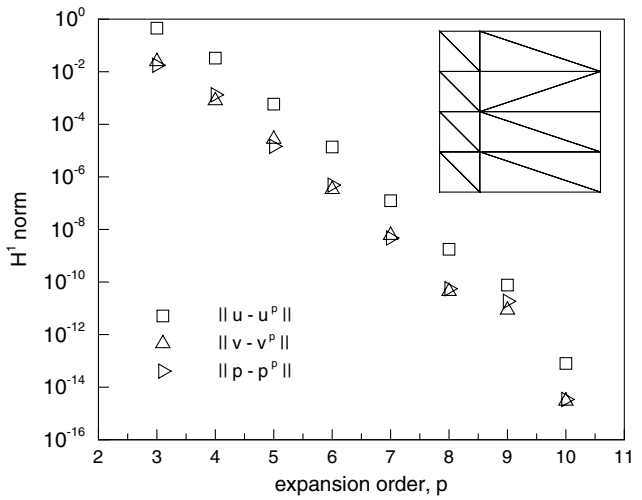

Fig. 3. Convergence of the velocity and pressure fields to the Kovasznay solution in the H^1 norm. Even and odd p-level error measures are for the mesh of triangles.

This is a pure-velocity Dirichlet problem, where no slip boundary conditions, $u = v = 0$, are prescribed on the two side-walls, $v = 0$ on the lid surface, and a regularized u-velocity distribution is prescribed on the lid; which drives the flow in the wedge. The u-velocity on the driven surface is a hyperbolic tangent u-velocity distribution:

$$u_{\mathrm{lid}}(x) = \begin{cases} \tanh(\beta(x+\sqrt{3})) & -\sqrt{3} \leqslant x \leqslant 0 \\ -\tanh(\beta(x-\sqrt{3})) & 0 < x \leqslant \sqrt{3} \end{cases}$$

with $\beta > 0$. Here we take $\beta = 50$, which gives a smooth but at the same time sharp transition from $u = 0.0$ to $u = 1.0$ near the walls of the driven surface. This boundary condition results in a well-posed boundary condition, in the sense that singularities at the corners of the driven surface are suppressed. It closely emulates the standard (ill-posed) boundary condition where no transition is allowed between the no-slip and the lid-driven velocity. A pressure datum, $p = 0$, is prescribed at the apex of the wedge to remove the pressure null-space of the pure-velocity Dirichlet problem.

We consider flow conditions corresponding to increasing Reynolds numbers and use the three successively finer meshes shown in Fig. 4. As the Reynolds number is increased the flow field inside the wedge displays richer flow physics, and increasing resolution is needed. Here we take the dual path of h- and p-refinements, where in addition to increasing the order of the polynomial basis inside each triangle (p-refinement), the number of triangles in the mesh is increased (h-refinement). The meshes M_1, M_2, and M_3 in Fig. 4 have 34, 86, and 199 triangles, respectively.

We use the stationary form of the equations and use a continuation technique with respect to the Reynolds numbers to compute the flow fields starting with $Re = 100$, with increments of 100. Typically only 3 Newton linearization steps are needed to compute the flow field at a given Reynolds number.

Fig. 5 shows vorticity contours of the flow field and the u-velocity distribution along the vertical center-line of the wedge at p-levels of 10 and 12, for Reynolds numbers $Re = 100$, 500, and 10^3 in the meshes M_1, M_2, and M_3, respectively. Fig. 6 shows streamlines of the flow fields up to $Re = 2 \times 10^3$, computed by solving $-\Delta\psi = \omega_z$ for the stream-function ψ in a post-processing stage. As the Reynolds number is increased additional recirculation regions appear in the wedge, indicative of the richer flow physics.

The velocity distributions along the vertical center-line in Fig. 5 are compared against tabulated data in [10], where the same problem was solved using over 40,000 (low-order) triangles with an upwinding scheme. Good agreement is found, although we predict higher peak velocities. The lower peak velocities reported in [10] are consistent with the dissipative nature of low-order elements and upwinding schemes. This brings up one of the nice features of least-squares formulations which need no stabilization (i.e. upwinding) for singularly perturbed problems, such as the high Reynolds number limiting cases.

Another nice property we wish to emphasize is that no special care is needed when numbering the global degrees of freedom. We use a matrix-free preconditioned conjugate gradient (PCG) algorithm, which is insensitive to the way the degrees of freedom are numbered, as no matrix storage or explicit matrix manipulations are required. The use of the matrix-free PCG solver is arguably optimal, as the resulting system of linear algebraic equations is SPD. Other solution approaches, such as algebraic multigrid methods [7] are possible as well. This is unlike the traditional implementation of the spectral element method [9], where interior degrees-of-freedom are statically condensed using linear algebra on dense element-level matrices, so that a

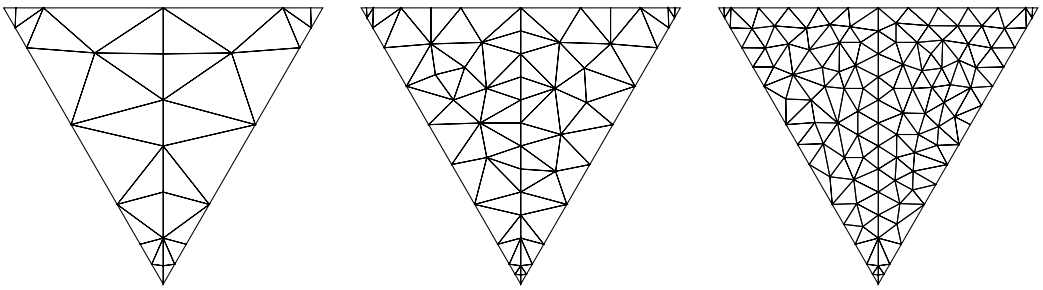

Fig. 4. Successively refined meshes M_1, M_2, and M_3 for the lid-driven flow in a wedge. The wedge is a $2\sqrt{3}$ equilateral triangle.

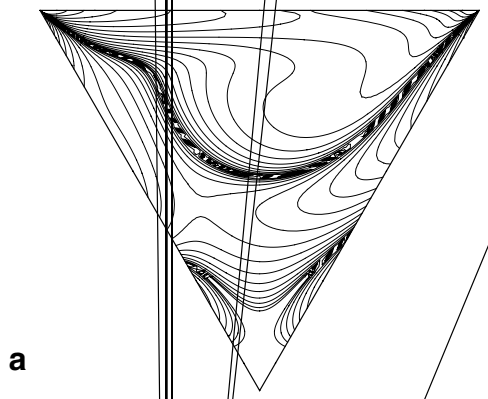

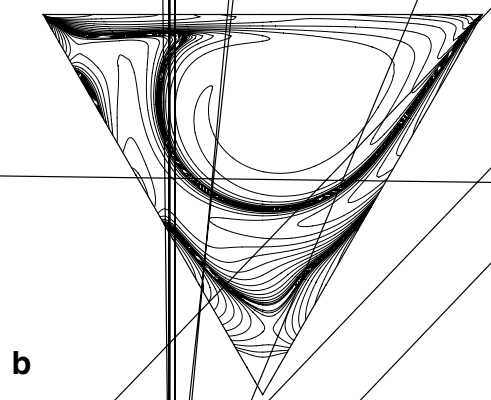

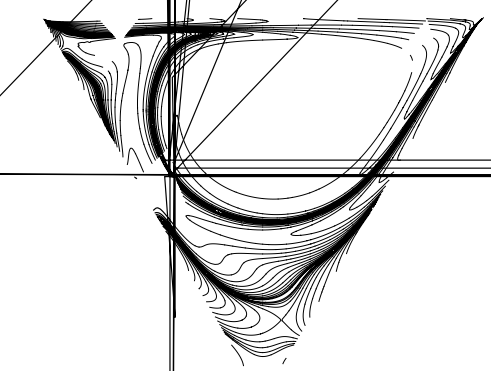

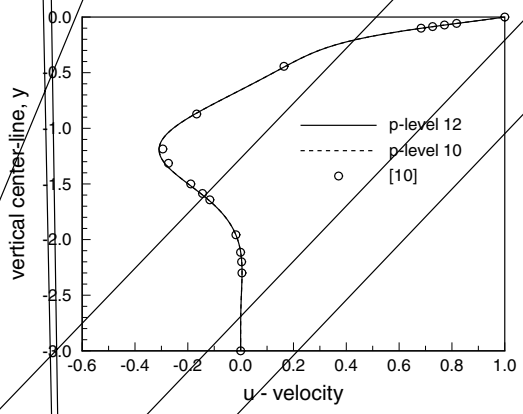

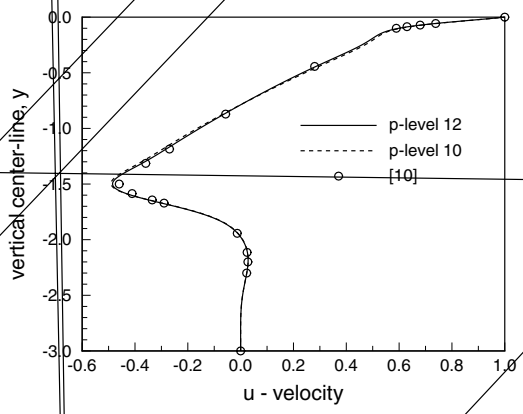

smaller sparse interface problem remains. Such an approach is always tied to a specific degree of freedom numbering scheme, to efficiently form and solve the interface problem.

4.3. A model problem to test conservation of mass

This is the model problem of Chang and Nelson [2] where a cylinder of unit diameter is moving in a very narrow channel, and is used here to test for conservation of mass. We first consider the original problem of Chang and Nelson [2], where the Stokes equations are solved. We then present results for unsteady flow governed by the Navier–Stokes equations, to test for conservation of mass in time.

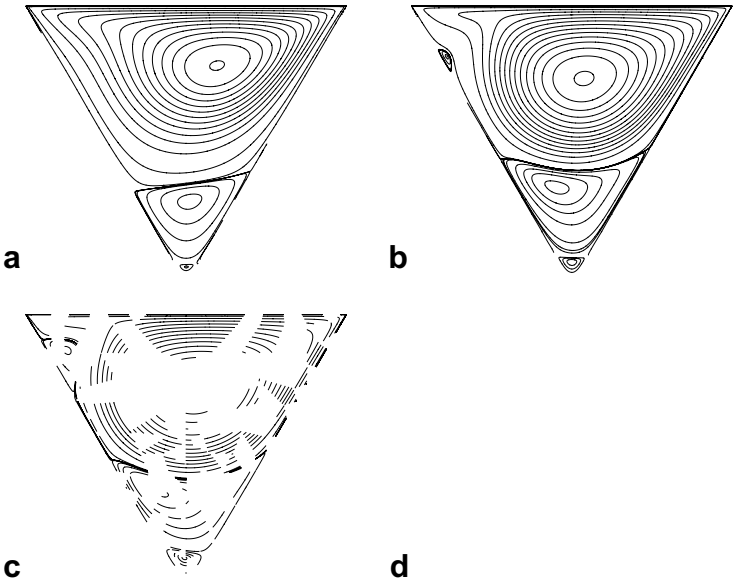

Fig. 6. Streamlines of the flow field for (a) $Re = 100$, (b) $Re = 500$, (c) $Re = 10^3$, and (d) $Re = 2 \times 10^3$.

The finite element mesh in the geometry of Chang and Nelson [2] consists of 96 triangles and is shown in Fig. 7. The boundary conditions are $u = 1$, $v = 0$ at the upstream and lateral boundaries and no-slip boundary conditions, $u = v = 0$, at the cylinder surface. Outflow boundary conditions are imposed in a weak sense through the least-squares functional [14,15]. For an outflow boundary whose unit normal is aligned with the x-axis, the outflow boundary conditions are:

$$-p + \frac{1}{Re}\frac{\partial u}{\partial x} = 0, \quad \frac{1}{Re}\frac{\partial v}{\partial x} = 0$$

4.3.1. Stokes flow

The governing equations for Stokes flow are obtained by simply setting $Re = 1$ and omitting the transient term and velocity nonlinearities in the Navier–Stokes equations. Mass flow rates are computed at the crown of the cylinder, where the gap between the channel walls and cylinder surface is the smallest, and at the outflow of the channel. At a p-level of 6, $\dot{m}_{\text{crown}}/\dot{m}_{\text{in}} = 0.979$ and $\dot{m}_{\text{out}}/\dot{m}_{\text{in}} = 0.978$. This corresponds to a 2.2% mass loss.

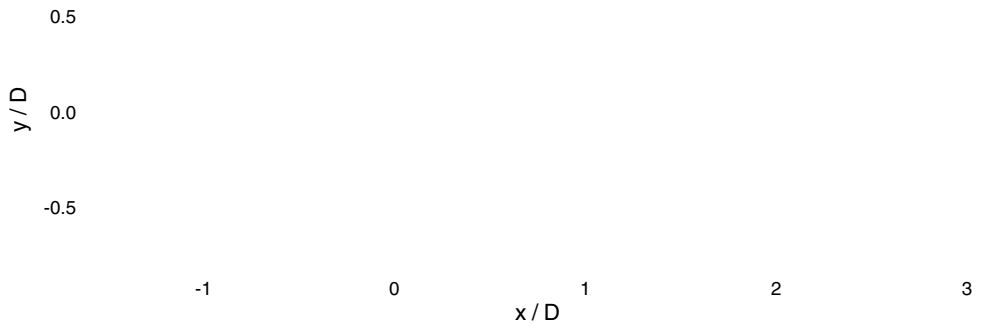

Fig. 7. Computational domain and mesh for the model problem to test for conservation of mass, due to Chang and Nelson [2].

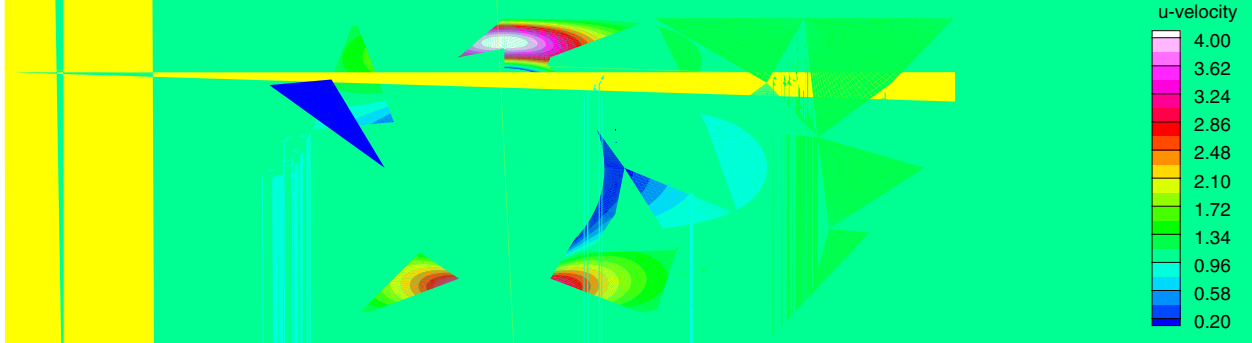

Fig. 8. *u*-velocity contours for Stokes flow in the channel, *p*-level 8.

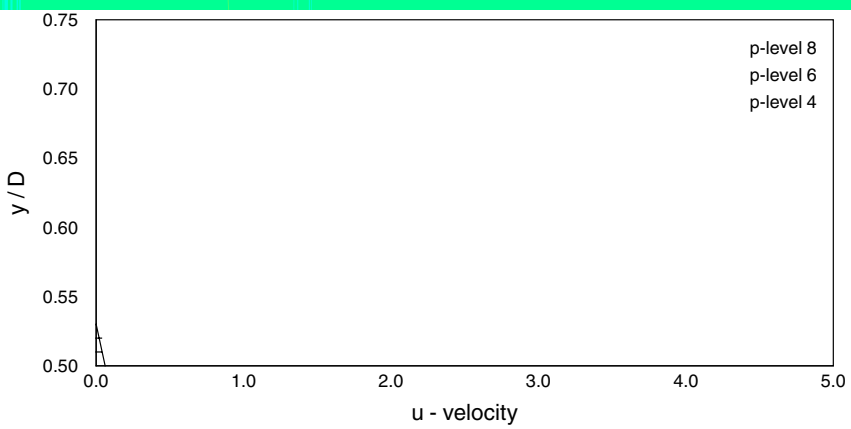

Fig. 9. *u*-velocity profile at the crown of the cylinder for Stokes flow in the channel, *p*-refinement.

4.3.2. Unsteady Navier–Stokes flow

The Reynolds number considered is $Re = 100$. The upper channel wall is shifted up by 0.03 units to promote the desired unsteadiness and the outflow boundary is moved downstream by 5.0 units to allow the wake to become well-developed.

We find that the vortex shedding occurs at a well-defined period of 1.88 time units. To adequately resolve the temporal evolution of the flow field we use $\Delta t = 0.02$, which gives a temporal resolution allowing for slightly over 90 time steps per shedding cycle.

The unsteady problem is more difficult in terms of velocity–pressure coupling and conservation of mass, as the pressure evolution in time must be such that mass is conserved at all times. Fig. 10a shows time histories of the mass flow rates at the crown cross-section and at the outlet of the channel for $t \in [190, 200]$, by which time the flow has well attained its periodic unsteady state. The expected response is $\dot{m}/\dot{m}_{\text{in}} = 1.0$ at all times.

From Fig. 10a we see that excellent conservation of mass is achieved. Note that the scale on which the mass flow rates are plotted allows for a maximum deviation of $\pm 2.0\%$ mass loss/gain, which is never reached. From Fig. 10a we see that the deviation from $\dot{m}/\dot{m}_{\text{in}} = 1.0$ is at all times negligible.

Fig. 10b shows the time history of the drag force exerted on the cylinder by the oncoming fluid. We compare our results with those reported in [16] for the same problem, obtained using quadrangles and a BDF3 time stepping scheme, by plotting the time histories alongside and find excellent agreement.

4.4. Unsteady flow past two circular cylinders

The flexibility of using triangles to partition a domain is further demonstrated in this last numerical example, where we consider the unsteady flow past two circular cylinders in a side-by-side arrangement. Both cylinders are equal in size, with diameter D, and face the free-stream. The flow around such an arrangement is characterized by distinct flow regimes, depending on the gap size S between cylinder surfaces [21,22].

Here we consider a gap size $S/D = 0.85$ and flow conditions $Re = 100$, based on the free-stream velocity and cylinder diameter. For this gap size, the flow through the gap is diverted towards one side or the other and the vortex wake becomes distinctly asymmetric. In addition, gap vortices are amalgamated with dominant outer vortices leading to the formation of a single large-scale vortex street [21].

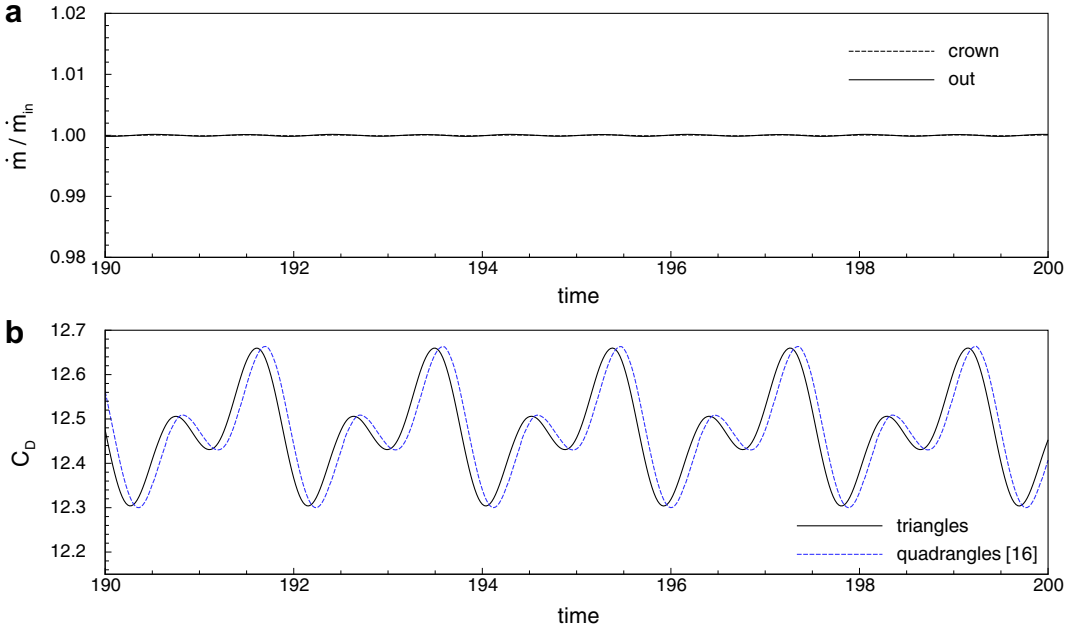

Fig. 10. Unsteady Navier–Stokes flow, BDF2 time stepping and p-level 8. (a) Time history of mass flow rates at the crown and outlet showing zero mass loss in time. (b) Time history of the drag force exerted on the cylinder.

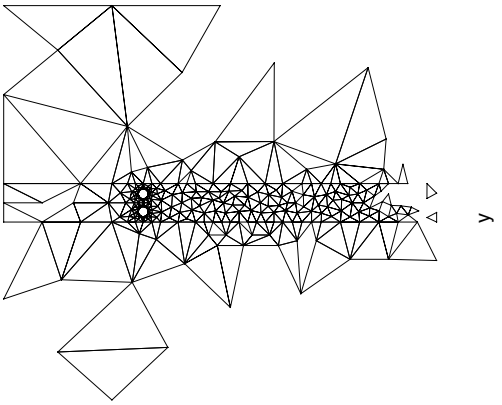

The finite element mesh used for the computation consists of 561 triangles and is shown in Fig. 11. In the far-field, where the solution will be fairly smooth, we use large triangles whereas in the wake region and in the gap, where smaller scales will be present, we use smaller triangles. The p-level in each triangle is set to 8 and the time step size is set to $\Delta t = 0.05$.

The size of the computational domain is taken sufficiently large to preclude unwanted effects on computed flow metrics due to blockage, or location of inflow and outflow boundaries. The circular cylinders are of unit diameter, with their centers located at $(x, y) = (0, -0.925)$ and $(0, 0.925)$, and are placed in the rectangular region $\bar{\Omega} = [-14.5, 30.5] \times [-20.5, 20.5]$.

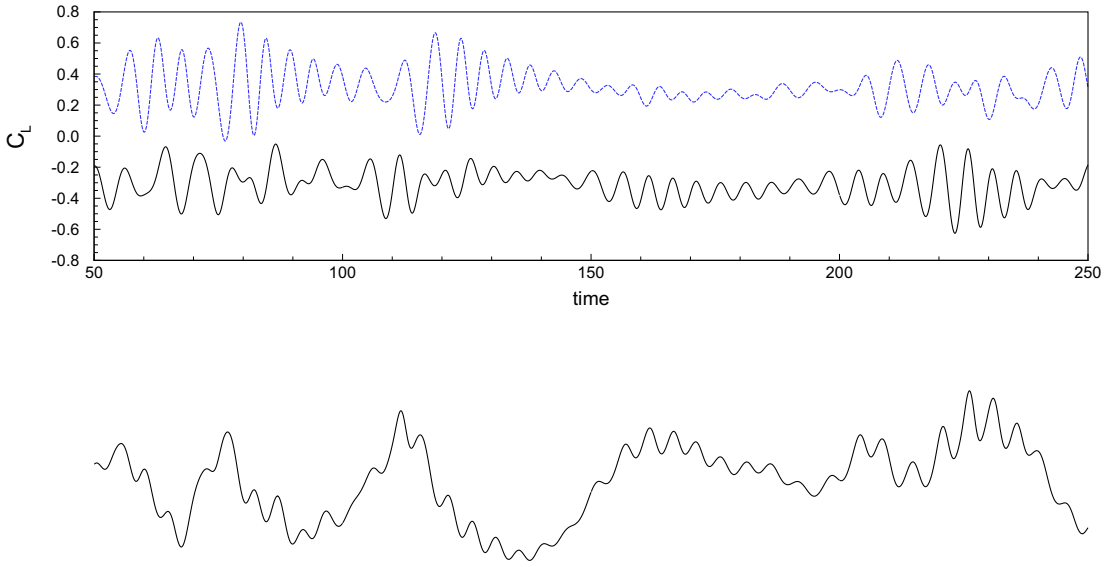

At this gap size, we did not see (or expected) a well-defined periodic steady state. The simulation was thus carried out for $t \in [0, 250]$, by which time the flow exhibited "well-developed" characteristics such as intermittent bistable gap jets and amalgamation of gap vortices leading to the formation of a single large-scale vortex street.

Fig. 12 shows instantaneous vorticity contours at $t = 200$ and $t = 250$. In accordance with the experimental visualizations of Williamson [21], a single large-scale vortex street is formed downstream of the cylinders; by virtue of vortex interactions in the near-wake of the cylinders. Gap vortices from both cylinders are squeezed and amalgamated with dominant outer vortices.

Fig. 13 shows the time history of the lift and drag forces exerted on the cylinders by the flow field. In accordance with experimental observations, there exists a mean repulsive (lift) force between the cylinders. The forces do not display a single well-defined frequency, but show harmonic behavior at different frequencies which vary in time.

5. Summary and concluding remarks

We presented a spectral element least-squares formulation for incompressible flows using a C^0 triangle based spectral nodal basis. For unsteady flows, time stepping was performed using a second-order BDF scheme. Numerical examples using a FOSLS formulation with vorticity as an auxiliary variable were presented. The spectral convergence property was verified for smooth solutions and excellent conservation of mass was observed for steady and unsteady problems. The flexibility of using triangles to partition geometries where the use of quadrangles would be problematic and/or inefficient was demonstrated in lid-driven flows in a wedge and flow past two circular cylinders in a side-by-side arrangement.

We conclude by making the following remarks regarding conservation of mass in least-squares formulations for the (un-split) incompressible Navier–Stokes equations. For the *stationary form of the equations*, good conservation of mass is due to the use of high p-levels (in either quadrangles or triangles). If one uses the regularized form of the divergence-free constraint, equally good conservation of mass and equally accurate numerical results are observed.

For the *non-stationary form of the equations*, good conservation of mass is due to the use of high p-levels (in either quadrangles or triangles) and the use of the regularized form of the divergence-free constraint. For non-stationary (i.e. unsteady) problems, we observe that a strong velocity–pressure coupling is necessary in order to maintain good conservation of mass in time – and the regularized form of the divergence-free constraint is used to ensure this strong coupling [16].

Acknowledgments

The ''macro-mesh'' triangulations in this work were generated using TRIANGLE; thanks to J.R. Shewchuk for making the code available. Computations were performed using resources of the Texas A&M Super Computer Facility; their support is acknowledged.

References

[1] L. Bos, M.A. Taylor, B.A. Wingate, Tensor product Gauss–Lobatto points are Fekete points for the cube, Math. Comput. 70 (2001) 1543–1547.
[2] C.L. Chang, J.J. Nelson, Least-squares finite element method for the Stokes problem with zero residual of mass conservation, J. Numer. Anal. 34 (1997) 480–489.
[3] M. Dubiner, Spectral methods on triangles and other domains, J. Sci. Comput. 6 (1991) 345–390.
[4] V. Girault, P. Raviart, Finite Element Methods for Navier–Stokes Equations, Springer-Verlag, New York, 1986.
[5] M.D. Gunzburger, Finite Element Methods for Viscous Incompressible Flows, Academic Press, New York, 1989.
[6] W. Heinrichs, Least-squares spectral collocation for the Navier–Stokes equations, J. Sci. Comput. 21 (2004) 81–90.
[7] J.J. Heys, T.A. Manteuffel, S.F. McCormick, L.N. Olson, Algebraic multigrid for higher-order finite elements, J. Comput. Phys. 204 (2005) 520–532.
[8] B.N. Jiang, The Least-squares Finite Element Method, Springer-Verlag, New York, 1998.
[9] G.E. Karniadakis, S.J. Sherwin, Spectral/*hp* Element Methods for CFD, Oxford University Press, Oxford, 1999.
[10] H. Kohno, K.J. Bathe, A flow-condition-based interpolation finite element procedure for triangular grids, Int. J. Numer. Meth. Fluids 49 (2005) 849–875.
[11] L.I.G. Kovasznay, Laminar flow behind a two-dimensional grid, Proc. Cambridge Phil. Soc. 44 (1948) 58–62.
[12] R. Pasquetti, F. Rapetti, Spectral element methods on triangles and quadrilaterals: comparisons and applications, J. Comput. Phys. 198 (2004) 349–362.
[13] A.T. Patera, A spectral element method for fluid dynamics: laminar flow in a channel expansion, J. Comput. Phys. 54 (1984) 468–488.
[14] J.P. Pontaza, J.N. Reddy, Spectral/*hp* least-squares finite element formulation for the Navier–Stokes equations, J. Comput. Phys. 190 (2003) 523–549.
[15] J.P. Pontaza, J.N. Reddy, Least-squares finite element formulations for viscous incompressible and compressible fluid flows, Comput. Meth. Appl. Mech. Eng. 195 (2006) 2454–2494.
[16] J.P. Pontaza, A least-squares finite element formulation for unsteady incompressible flows with improved velocity–pressure coupling, J. Comput. Phys. 217 (2006) 563–588.
[17] M.M.J. Proot, M.I. Gerritsma, Least-squares spectral elements applied to the Stokes problem, J. Comput. Phys. 181 (2002) 454–477.
[18] S.J. Sherwin, G.E. Karniadakis, A triangular spectral element method; applications to the incompressible Navier–Stokes equations, Comput. Meth. Appl. Mech. Eng. 123 (1995) 189–229.
[19] M. Taylor, B.A. Wingate, R.E. Vincent, An algorithm for computing Fekete points in the triangle, SIAM J. Numer. Anal. 38 (2000) 1707–1720.
[20] T. Warburton, L.F. Pavarino, J.S. Hesthaven, A pseudo-spectral scheme for the incompressible Navier–Stokes equations using unstructured nodal elements, J. Comput. Phys. 164 (2000) 1–21.
[21] C.H.K. Williamson, Evolution of a single wake behind a pair of bluff bodies, J. Fluid Mech. 159 (1985) 1–18.
[22] M.M. ZdravkovichFlow Around Circular Cylinders, vol. 2, Oxford University Press, Oxford, 2003.